Letter | Editors' Suggestion

Nonexponential relaxation in the rotating frame of a driven nanomechanical mode

Hyunjin Choi [1], Oriel Shoshani [2,*], Ryundon Kim [1], Younghun Ryu [1,†], Jinhoon Jeong [1,‡], Junho Suh [3], Steven W. Shaw [4,5,6], M. I. Dykman [6], and Hyoungsoon Choi [1,7,§]

[1]*Department of Physics, Korea Advanced Institute of Science and Technology (KAIST), Daejeon 34141, Republic of Korea*
[2]*Department of Mechanical Engineering, Ben-Gurion University of the Negev, Be'er-Sheva 84105, Israel*
[3]*Department of Physics, Pohang University of Science and Technology (POSTECH), Pohang 37673, Republic of Korea*
[4]*Department of Mechanical and Civil Engineering, Florida Institute of Technology, Melbourne, Florida 32901, USA*
[5]*Department of Mechanical Engineering, Michigan State University, East Lansing, Michigan 48824, USA*
[6]*Department of Physics and Astronomy, Michigan State University, East Lansing, Michigan 48824, USA*
[7]*Graduate School of Quantum Science and Technology, Korea Advanced Institute of Science and Technology (KAIST), Daejeon 34141, Republic of Korea*

(Received 24 August 2025; revised 3 November 2025; accepted 5 January 2026; published 2 February 2026)

We present direct observation of the ringdown dynamics in the rotating frame of a resonantly driven single-mode nonlinear nanomechanical resonator. An additional close-to-resonance harmonic force excites nonlinear oscillations about the fixed point in the rotating frame. When the secondary drive is removed, we measure decay of the in-phase and quadrature components toward this fixed point. We show that the decay of the in-phase signal is nonexponential, even though the vibration amplitude decays exponentially if both forces are switched off, revealing an unexpected interplay between conservative nonlinearity and dissipation. A minimalistic model captures these dynamics as well as the spectrum of the vibrations excited by the additional force, relating them to the dissipation-induced symmetry breaking of the dynamics in the rotating frame.

DOI: 10.1103/xhll-lhcj

Decay of vibrations of nanomechanical systems reveals important information about the physics of the vibrational modes, such as their linear or nonlinear coupling to other excitations, including the mode-mode coupling. The decay rate imposes the limits on various applications of the mechanical modes, in particular those in classical and quantum sensing. [1–5]. Measuring the spectral linewidth is usually sufficient to determine the decay rate of many vibrational systems, especially at macro- and microscales. However, in nanomechanical systems, spectral linewidths can be broadened by frequency fluctuations, obscuring the true decay rate [6–9]. To overcome this limitation, ringdown measurements are widely adopted [3,10–13].

In a ringdown measurement, the system is actively driven initially, then the drive is turned off, and the resulting change in energy or amplitude over time is directly tracked. This transient response allows one to separate out dissipation from dephasing effects [14]. A major dissipation mechanism in nanomechanical systems is the coupling to a thermal reservoir, which is linear in the mode coordinate; it leads to a rather simple exponential decay of the amplitude [5]. However, the decay due to nonlinear coupling [15] may be more complicated, and ringdown measurements can detect such interesting characteristics of the systems as nonlinear (amplitude-dependent) damping, nonlinear frequency shifts, and mode coupling [3,13,16–19].

The rotating frame offers a simple view of intricate nonlinear dynamics and is widely used when analyzing nanomechanical oscillators. In this frame, a sinusoidal response to a resonant drive is described by a fixed point. Studying vibrational dynamics in the rotating frame has unearthed a wealth of phenomena, including fluctuation squeezing [20–22], the onset of spectral sidebands [23,24], frequency combs [25–32], the occurrence of chaos [33,34], and manifestations of mode coupling [35–39]. However, the relaxation from an excited state to the fixed point in the rotating frame has remained largely unexplored.

In this Letter, we tackle the problem of decay directly by studying the ringdown of a nanomechanical system in the rotating frame. We find that a driven nonlinear nanomechanical oscillator with a very small damping exhibits an unexpected behavior: A conservative nonlinearity leads to nonexponential decay in the rotating frame, even though, in the absence of a drive, the decay remains exponential in the laboratory frame. The effect is pronounced even where the nonlinear part of the vibration energy in the laboratory frame remains small compared to the linear part.

Our system is subjected to a near-resonant harmonic drive in the laboratory frame, which can be used to tune the dynamics in the rotating frame. The harmonic drive breaks the time-translational symmetry of the system. It provides a refer-

*Contact author: oriels@bgu.ac.il
†Present address: Institute of Physics and Center for Quantum Science and Engineering, École Polytéchnique Fédérale de Lausanne (EPFL), Lausanne 1015, Switzerland.
‡Present address: QTF Centre of Excellence, Department of Applied Physics, Aalto University, FI-00076 Aalto, Finland.
§Contact author: h.choi@kaist.ac.kr

ence for studying the response to a weak secondary drive that we apply. Viewed in the rotating frame, the secondary drive perturbs the system into a state of forced periodic vibrations about the fixed point. They manifest as a frequency comb in the laboratory frame [26,27].

By turning off the secondary drive, we observe the ringdown, i.e., relaxation towards the fixed point in the rotating frame. The ringdown response shows different decay patterns for the in-phase and quadrature components owing to the nonlinearity, which is strong in the rotating frame, while is still weak in the laboratory frame. The distinct decay rates observed for the in-phase and quadrature components are ultimately related to the lack of symmetry with respect to time translation by a quarter of the modulation period, which would lead to the interchange of the components. In addition, the system lacks inversion symmetry in the rotating frame, which, as we show, results in significant contributions of even harmonics to the frequency content of the dynamical variables—a revealing signature of the underlying strong nonlinearities.

The system we study is a doubly clamped beam in a tensile-stress dominated regime [40,41]. The device is a heterostructure composed of 100 − nm-thick silicon nitride and a 50 − nm-thick aluminum layer deposited on top for carrying an alternating current. The beam is $L = 360$ μm long and $w = 1$ μm wide, as shown in Fig. 1(a). The bare mass of the wire from its physical dimension is $m = 1.63 \times 10^{-13}$ Kg. The device is housed in an experimental cell and cooled to approximately $T \approx 4$ K. The low-vacuum environment ($\sim 10^{-6}$ mbar) ensures low-damping conditions.

We focus on the fundamental flexural mode of the nanoresonator. Its dynamics is well described by the following minimalistic model:

$$\ddot{x} + 2\Gamma\dot{x} + \omega_0^2 x + \gamma x^3 = F_1 \cos(\omega_1 t) + F_2 \cos(\omega_2 t), \quad (1)$$

where x is the modal displacement, Γ, ω_0, and γ are the damping, natural frequency, and Duffing coefficients of the mode, respectively, and we use units where the mode mass is set equal to 1. Except for special cases [42], this model describes response to a resonant drive even where the system does not have inversion symmetry [43], and it works well in our case, as seen in Fig. 1. The primary and secondary forces on the right-hand side of Eq. (1) have drive amplitudes F_1 and F_2, and drive frequencies ω_1 and ω_2, respectively. While the driving frequencies, ω_1 and ω_2, are kept close to the mode eigenfrequency, the magnitude of the forces differs significantly, with $F_1 \gg F_2$, and hence F_1 is designated as the primary drive.

The measured eigenfrequency of the mode is $\omega_0/2\pi \approx 248.013$ kHz [see the inset of Fig. 1(b)]. When the drive is turned off, we observe exponential decay of the vibration amplitude during the ringdown in the Duffing nonlinear regime, with the slope Γ on a log-linear plot depicted in Fig. 1(c). This slope gives the relaxation rate $\Gamma = 1.35$ Hz ($Q \approx 580\,000$). During the ringdown, the vibration frequency, which is amplitude dependent due to the Duffing nonlinearity, approaches ω_0. Figure 1(b) illustrates a Duffing stiffening response, which reveals the familiar frequency dependence on the vibration amplitude. The Duffing nonlinearity is quantified from the backbone curve; using $\omega_{\max} - \omega_0 = 3\gamma a_{\max}^2/(8\omega_0)$, where $\omega_{\max}$ and $a_{\max}$ are the maximal values of frequency

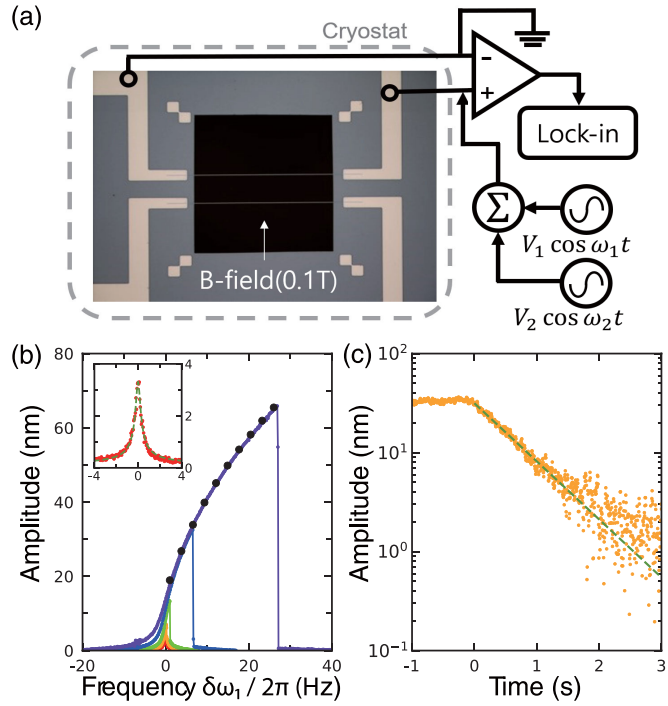

FIG. 1. (a) Optical image of the resonator and measurement setup. The experiment is conducted on one of the two suspended strings. (b) The nonlinear resonance curves in the laboratory frame of the first flexural mode were obtained from upward frequency sweeps. The rainbow-colored curves represent measured amplitude spectra at increasing drive strengths. The black dots represent the theoretical approximation values along the curve. The inset shows a resonance curve in the linear regime with drive $F_1 = 0.015$ m/s^2, and the green dashed curve represents a fit to the amplitude response of a driven damped harmonic oscillator. (c) Ringdown response of the first flexural mode amplitude in the Duffing nonlinear regime under a drive of $F_1 = 0.15$ m/s^2 and $\delta\omega_1/2\pi = 6.5$ Hz. The green dashed line represents the fitted linear decay.

and amplitude reached on the response curve [Fig. 1(b)], we obtain $\gamma = 1.597 \times 10^{23}$ m^{-2} s^{-2} With the experimentally evaluated Γ, ω_0, and γ, we find the following critical drive level for the onset of bistability: $F_{\mathrm{cr}_1} = 16\sqrt{\omega_0^3\Gamma^3/(9\sqrt{3}\gamma)} = 0.033$ m/s^2 [43].

Our primary interest lies in the rotating frame dynamics associated with the large-amplitude branch of the Duffing oscillator, as described by Eq. (1), in the regime where $F_2 \ll F_1$ and $|\omega_2 - \omega_1|/\omega_0 \ll 1$. We change variables to q, p using $x(t) = q(t)\cos(\omega_1 t) + p(t)\sin(\omega_1 t)$ and the corresponding equation for $\dot{x}$. Then, we obtain in the rotating-wave approximation (RWA) the following Hamiltonian $\mathcal{H} = \mathcal{H}_0(q,p) + \mathcal{H}_1(q,p,t)$, where

$$\mathcal{H}_0(q,p) = \frac{3\gamma}{32\omega_1}(q^2+p^2)^2 - \frac{1}{2}\delta\omega_1(q^2+p^2) - \frac{F_1 q}{2\omega_1},$$

$$\mathcal{H}_1(q,p,t) = -F_2[q\cos(\delta\omega_2 t) - p\sin(\delta\omega_2 t)]/2\omega_1,$$

and the frequency detunings are given by $\delta\omega_1 = \omega_1 - \omega_0$, $\delta\omega_2 = \omega_2 - \omega_1$. The second frequency detuning, $\delta\omega_2$, is defined relative to ω_1 rather than ω_0, as the rotating frame is

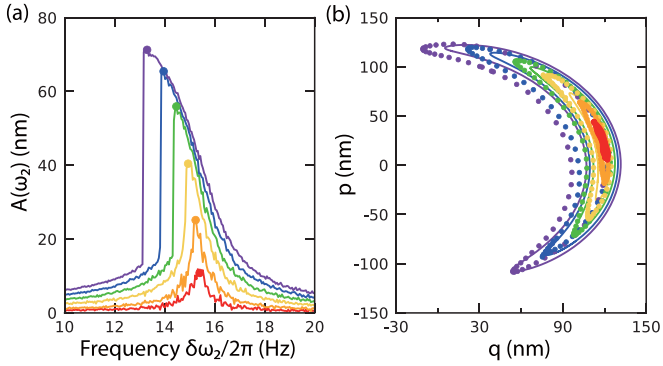

FIG. 2. (a) The amplitude $A(\omega_2)$ of vibrations for downward frequency sweeps of the secondary-drive frequency ω_2, measured at $F_2 = 15,\ 30,\ 60,\ 90,\ 120,$ and 150mm/s^2, with F_1 fixed at $3.0\ \text{m/s}^2$. The signal $A(\omega_2)$ is plotted against the detuning $\delta\omega_2 = \omega_2 - \omega_1$ of the secondary drive. The peak values of the amplitudes for different F_2 are marked with solid circles. (b) The measured (circles) phase-space trajectories of $(q,\ p)$ in the rotating frame for the frequencies ω_2 corresponding to the maximal $A(\omega_2)$ in (a), with the matching color coding. The trajectories are obtained by homodyne measurement with reference frequency at ω_1. Rainbow-colored curves are obtained by numerically solving the equations $\dot{q} = \partial_p \mathcal{H} - \Gamma q$ and $\dot{p} = -\partial_q \mathcal{H} - \Gamma p$ for the corresponding sets of $(F_2, \delta\omega_2)$.

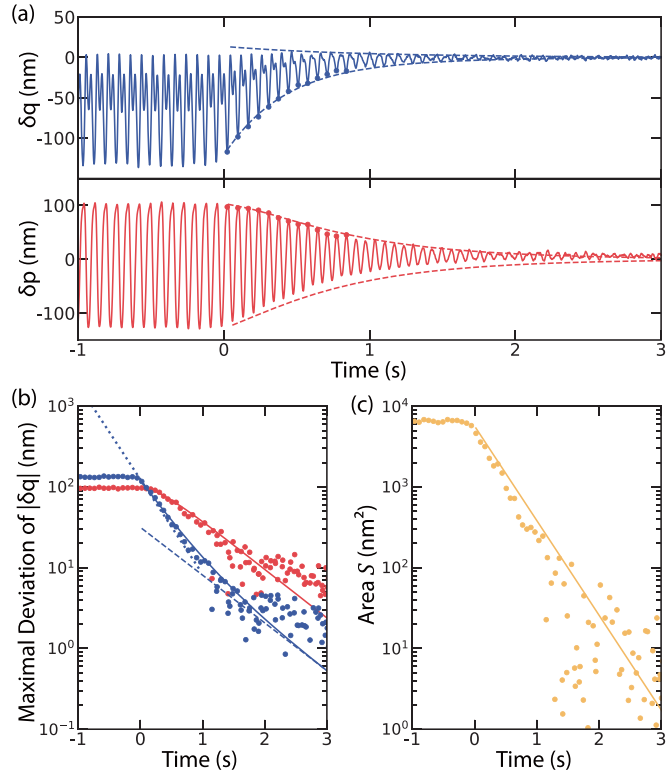

FIG. 3. (a) The ringdown signals of $\delta q = q(t) - q_{\text{eq}}$ and $\delta p = p(t) - p_{\text{eq}}$. The system is initially driven by the secondary drive with $\delta\omega_2/2\pi = 13$ Hz and $F_2 = 150\ \text{mm/s}^2$, while the primary resonant drive is set at $\delta\omega_1/2\pi = 86.9$ Hz and $F_1 = 3.0\ \text{m/s}^2$. F_2 is switched off at $t = 0$. Dashed blue and red curves represent, respectively, theoretical predictions for the ringdown envelopes of δq and δp. (b) Log-linear plot of the maximal deviations for δq (blue) and δp (red). Solid curves show the theoretical predictions for the maximal displacement of the vibrations $|\delta q(t)|$ and $|\delta p(t)|$. The blue dotted and dashed lines represent the decay rate 2Γ and Γ, respectively. (c) The decay of the area enclosed by phase-space trajectories in the rotating frame over time. Yellow circles indicate the experimental data and the yellow curve is the theoretical prediction.

chosen at frequency ω_1. From Eq. (1), we obtain the RWA equations of motion for q, p of the form $\dot{q} = \partial_p \mathcal{H} - \Gamma q$, $\dot{p} = -\partial_q \mathcal{H} - \Gamma p$.

When $F_2 = 0$, and if we disregard damping, the mode performs vibrations in the rotating frame about the fixed point $(q_{\text{eq}}, p = 0)$, with q_{eq} being the larger solution of the equation $F_1/(2\omega_1) + \delta\omega_1 q_{\text{eq}} - 3\gamma q_{\text{eq}}^2/(8\omega_1) = 0$. Where the amplitude of these vibrations is small, their frequency is given by $\Omega = \sqrt{\omega^{(1)}\omega^{(2)}}$, with $\omega^{(1)} = \partial_p^2 \mathcal{H}|_{q_{\text{eq}}} = (3\gamma q_{\text{eq}}^2/(8\omega_1) - \delta\omega_1)$, $\omega^{(2)} = \partial_q^2 \mathcal{H}|_{q_{\text{eq}}} = (9\gamma q_{\text{eq}}^2/(8\omega_1) - \delta\omega_1)$. The weak damping of our system allows us to consider the regime where Γ is small, not only compared to ω_0, but also compared to Ω, i.e., the vibrations are underdamped in the rotating frame.

In the absence of damping ($\Gamma = 0$) and secondary drive ($F_2 = 0$), the equations of motion $\dot{q} = \partial_p \mathcal{H}_0$ and $\dot{p} = -\partial_q \mathcal{H}_0$ can be rewritten in terms of the scaled energy of a harmonic oscillator $I_{\text{HO}} \equiv (q^2 + p^2)/2$ (cf. Ref. [43]):

$$q = \frac{3\gamma}{4F_1} I_{\text{HO}}^2 - \frac{2\omega_1 \delta\omega_1}{F_1} I_{\text{HO}} - \frac{2\omega_1 \mathcal{H}_0}{F_1}, \quad p = \frac{2\omega_1}{F_1} \dot{I}_{\text{HO}}. \quad (2)$$

The time evolution of I_{HO} is determined by the first-order equation $\dot{I}_{\text{HO}}^2/2 + U_{\text{eff}}(I_{\text{HO}}) = 0$ with an effective potential U_{eff}, and can be described explicitly in terms of the Jacobi elliptic functions; see Supplemental Material [44]. It describes in the explicit form periodic oscillations of I_{HO}, and thus of the dynamical variables q, p, with frequency that depends on the value of $\mathcal{H}_0$. This solution allows us to analyze, in the rotating frame, the linear and nonlinear response of the mode to the secondary drive. In particular, it enables studying the analog of the "backbone" curve of such response.

In Fig. 2 we show the measured response of the oscillator to the secondary drive. We focus on the response at the drive frequency ω_2. For small F_2, the response is maximal at $\omega_2 = \omega_1 + \Omega$, and its amplitude $A(\omega_2)$ increases linearly with F_2. As the drive is further increased the response shows nonlinear behavior. Driving with F_2 beyond a critical value F_{cr_2} pushes the response curve $A(\omega_2)$ into a bistable regime, and a set of downward frequency-sweeping measurements reveals frequency pulling-away behavior, reminiscent of a softening Duffing response as shown in Fig. 2(a). This is caused by the dependence of the effective frequency of the vibrations in the rotating frame on the value of the Hamiltonian $\mathcal{H}_0$. The small rainbow-colored circles in the figure indicate the maximal amplitudes at each value of F_2. They determine the initial conditions of the ringdown measurements shown in Fig. 3, which are done by turning off F_2.

The phase-space trajectories of $(q,\ p)$ in the rotating frame are obtained by setting ω_2 to produce the peak amplitude at each drive level of F_2 and then carrying out a homodyne detection with the the primary drive at ω_1 as the reference; see Fig. 2(b). However, the trajectories do not have mirror-reflection symmetry with respect to the axis $p = 0$. This is

a consequence of dissipation, which breaks time-inversion symmetry.

Turning off the secondary drive F_2 induces ringdowns probed by homodyne measurements referenced at frequency ω_1. As depicted in Fig. 3(a), the quadratures decay to the equilibrium position $\delta q = q - q_{\rm eq} \to 0$, $\delta p = p - p_{\rm eq} \to 0$. To characterize this decay process, we identify the points of the maximal deviations as the point furthest away from the equilibrium on the phase-space trajectories in Fig. 2(b) during each cycle. A handful of these points are marked by the blue and red circles on the curves in Fig. 3(a). The points of the maximal deviations are then plotted against time in Fig. 3(b) to illustrate the decay process.

Two unexpected features immediately stand out from Fig. 3(b). The first is that the ringdown of δq shows a nonexponential decay. Second, the decays of q and p are not identical. The initial decay rates of q and p, i.e., where the deviations $|\delta q|$ and $|\delta p|$ are close to maximal, are measured to be 2.50 and,1.31 Hz, respectively. These values are in a good agreement with the decay rates of $\approx 2\Gamma$ and $\approx \Gamma$ calculated for the chosen parameters and indicated by the early-time slopes in Fig. 3(b). However, overall, the decay of q is profoundly nonexponential; the effective decay rate associated with the slope of $|\delta q|$ in Fig. 3(b) decreases in time from $\approx 2\Gamma$ to a smaller value, which is $\sim\Gamma$ (the data for small $|\delta q|$ are somewhat obscured by the noise; the analysis of this effect is presented in the Supplemental Material [44]).

The difference in the decay of the quadratures is rooted in the breaking of the continuous time translation symmetry by the periodic drive. Another manifestation of this asymmetry is the fluctuation squeezing observed in Ref. [20]. However, our ringdown measurements do not require the analysis of fluctuations to reveal the symmetry-breaking effect. We emphasize that this is temporal, not spatial, symmetry breaking that underlies the effect.

During the ringdown, because of the slow decay rate, the trajectories $q(t)$, $p(t)$ in the rotating frame form a tight spiral, with the ratio of the step to the characteristic radius $\lesssim 0.1$. One can then consider the approximate area $\mathcal{S}$ enclosed in a single turn of this spiral. In the absence of decay, this area would provide the action of conservative system with Hamiltonian $\mathcal{H}_0$. In the presence of decay, $\mathcal{S}$ decays as the mode approaches the fixed point. This decay is shown in Fig. 3(c). It is exponential at the rate of 2.69 Hz $\approx 2\Gamma$, consistent with our model. This should be contrasted with the strongly nonexponential decay of $q(t)$. We emphasize that we observe such nonexponential decay in a single-mode resonator, in contrast to multimode systems, where nonexponential decay is associated with intermode energy exchange, cf. Refs. [11,13]. We also emphasize that if the mode displayed nonlinear friction [5], the decay of $\mathcal{S}$ would be profoundly nonexponential.

We now discuss the spectra of the system in the presence of a secondary drive. In Fig. 4 we show the Fourier transforms of the coordinate and momentum in the rotating frame. The spectra display multiple peaks, which correspond to the overtones of the vibrations at frequency $\delta\omega_2$, $q(t) = \sum q_n \exp(in\delta\omega_2 t)$ and $p(t) = \sum p_n \exp(in\delta\omega_2 t)$. The occurrence of the overtones leads to a frequency comb in the laboratory frame, with the spectral lines of the comb located at frequencies $\omega_1 + n\delta\omega_2$ with integer n. The comb is pronounced at a

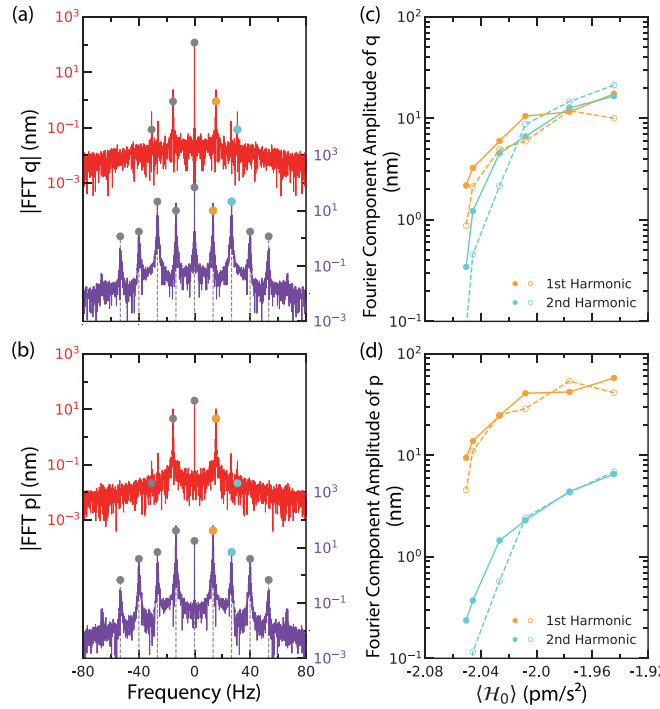

FIG. 4. (a), (b) Spectra of $q(t)$ and $p(t)$, obtained by fast Fourier transform of the outcomes of homodyne measurements for two values of the secondary drive $(\delta\omega_2/2\pi, F_2) = (15.4\ \text{Hz}, 15\ \text{mm/s}^2)$ (upper$(\delta\omega_2/2\pi, F_2) = (13.3\ \text{Hz}, 150\ \text{mm/s}^2)$ red) and $(\delta\omega_2/2\pi, F_2) = (13.3\ \text{Hz}, 150\ \text{mm/s}^2)$ (lower, purple). These values correspond to the two peak amplitudes marked by red and purple circles in Fig. 2(a), respectively, with F_1 also set to 3.0 m/s^2, the same values used for Fig. 2 and Fig. 3. Colored circles (gray, yellow, and cyan) at the peaks of the spectra are the theoretical values. (c), (d) Amplitudes of the first (yellow) and second (cyan) harmonics components of $q(t)$ and $p(t)$ as functions of the averaged Hamiltonian $\langle\mathcal{H}_0\rangle$ calculated for different F_2 and $\delta\omega_2/2\pi$. Filled circles and empty circles represent measured data and theoretical calculations, respectively. The solid and dashed lines between the circles are guides to the eye.

sufficiently strong F_2. It reveals a strong and nontrivial dependence of higher harmonics of $q(t)$ on the secondary drive. This dependence reflects the spectral composition of nonlinear vibrations in the rotating frame as functions of the vibration "energy" $\mathcal{H}_0$ in the absence of decay and F_2. It is therefore instructive to describe it using the values $\langle\mathcal{H}_0\rangle$, which are obtained by averaging $\mathcal{H}_0$ for given F_2, $\delta\omega_2$ along the experimental trajectory.

We find that the second harmonic of $q(t)$ becomes comparable to the first harmonic, i.e., $q_2/q_1 \sim 1$ already for $\langle\mathcal{H}_0\rangle \approx -1.98\ \text{pm}^2/\text{s}$, or for the secondary drive amplitude $F_2 \approx 120\ \text{mm/s}^2$ for $\delta\omega_2 = 13.96$ Hz, as shown in Fig. 4(c). In contrast, for the same parameters, in the spectrum of $p(t)$ only the first harmonic is pronounced; see Fig. 4(d). Such a difference in the behavior of two quadratures is distinct from the response of most weakly nonlinear systems, such as a system with a standard Duffing nonlinearity, where the second harmonic remains small up to fairly large vibration amplitudes; cf. Ref. [42].

There is a connection between the evolution of the decay rates during the ringdown shown in Fig. 3(b) and the frequency content of the quadratures shown in Fig. 4. In a quasilinear picture, the components $q_n(t)$ and $p_n(t)$ decay at rates $n\Gamma$. Then, if the dominating components of $q(t)$ and $p(t)$ are q_2 and p_1, respectively, one might expect that $q(t)$ will decay at the rate $\sim 2\Gamma$, and $p(t)$ will decay at the rate $\sim\Gamma$. This argument provides an insight into the decay rates at large amplitudes, where $|q_2| \sim |q_1|$, whereas $|p_2| \ll |p_1|$. The nonexponential decay is only visible when the ringdown is initiated from relatively large $\langle \mathcal{H}_0 \rangle$.

In conclusion, we experimentally investigated relaxation of a driven single-mode nonlinear nanomechanical resonator in the rotating frame. The nonlinearity is weak, and the vibration amplitude of the resonator decays exponentially in time, in the absence of a drive. However, we find that even conservative nonlinearity can modify the decay rate in the rotating frame, leading to distinctly nonexponential relaxation. The ringdown data that we collect show marked differences between the decays of the in-phase and quadrature components. Our results on the effect of a weak extra drive show the onset of a pronounced second-harmonic signal in the rotating frame, but only in the in-phase component. A minimalistic nonlinear model successfully describes the observations and reveals the relation between the nonexponential decay and the harmonic generation, which result from the interplay of the nonlinearity, dissipation, and the broken time-translation and time-inversion symmetry of the driven mode.

More broadly, because it requires minimal conditions, this effect is generic and likely to arise in a wide class of driven nonlinear oscillators. Furthermore, as we find, studying decay in the rotating frame offers a powerful tool for revealing and exploring nonlinear effects, as the scale on which the system becomes significantly nonlinear is much smaller than in the absence of the drive; cf. Ref. [5]. This is particularly valuable in high-Q nanomechanical systems, where conventional linewidth measurements might mask important details. By connecting spectral signatures to time-domain decay patterns, our approach provides a framework for interpreting nonexponential relaxation processes, and suggests ways of controlling nonlinear phenomena. Beyond the present setting, the technique can also serve as a means of probing different dissipative environments—for example, immersing the resonator in superfluid helium, where its vibration generate vortices [48–50]—to study the nontrivial interplay between nonlinearity and dissipation, offering a pathway to deeper understanding of the rich many-body physics of dissipation processes.

This work is supported by National Research Foundation of Korea (NRF) Grants No. RS-2022-NR070358, No. RS-2023-00207732, No. RS-2023-00256050, and No. RS-2025-25455172. O.S. is grateful for support from the Israel Science Foundation (ISF) Grant No. 344/22 and the Pearlstone Center of Aeronautical Engineering Studies at BGU. J.S. acknowledges additional supports from NRF and IITP (Grants No. RS-2022-00164799 and No. RS-2024-00352688). S.W.S. and M.I.D. acknowledge partial support from the Defense Advanced Research Projects Agency (DARPA) H6 program under Cooperative Agreement No. HR0011-23-2-0004.

Data availability. The data that support the findings of this article are not publicly available. The data are available from the authors upon reasonable request.

[1] K. L. Ekinci and M. L. Roukes, Nanoelectromechanical systems, Rev. Sci. Instrum. **76**, 061101 (2005).

[2] Q. P. Unterreithmeier, T. Faust, and J. P. Kotthaus, Damping of nanomechanical resonators, Phys. Rev. Lett. **105**, 027205 (2010).

[3] C. Chen, D. H. Zanette, D. A. Czaplewski, S. Shaw, and D. López, Direct observation of coherent energy transfer in nonlinear micromechanical oscillators, Nat. Commun. **8**, 15523 (2017).

[4] A. A. Clerk, M. H. Devoret, S. M. Girvin, F. Marquardt, and R. J. Schoelkopf, Introduction to quantum noise, measurement, and amplification, Rev. Mod. Phys. **82**, 1155 (2010).

[5] A. Bachtold, J. Moser, and M. I. Dykman, Mesoscopic physics of nanomechanical systems, Rev. Mod. Phys. **94**, 045005 (2022).

[6] O. Maillet, X. Zhou, R. Gazizulin, A. M. Cid, M. Defoort, O. Bourgeois, and E. Collin, Nonlinear frequency transduction of nanomechanical Brownian motion, Phys. Rev. B **96**, 165434 (2017).

[7] Y. Zhang and M. I. Dykman, Spectral effects of dispersive mode coupling in driven mesoscopic systems, Phys. Rev. B **92**, 165419 (2015).

[8] K. Y. Fong, Wolfram H. P. Pernice, and H. X. Tang, Frequency and phase noise of ultrahigh Q silicon nitride nanomechanical resonators, Phys. Rev. B **85**, 161410(R) (2012).

[9] L. Huang, S. M. Soskin, I. A. Khovanov, R. Mannella, K. Ninios, and H. B. Chan, Frequency stabilization and noise-induced spectral narrowing in resonators with zero dispersion, Nat. Commun. **10**, 3930 (2019).

[10] S. Schmid, K. D. Jensen, K. H. Nielsen, and A. Boisen, Damping mechanisms in high-Q micro and nanomechanical string resonators, Phys. Rev. B **84**, 165307 (2011).

[11] J. Güttinger, A. Noury, P. Weber, A. M. Eriksson, C. Lagoin, J. Moser, C. Eichler, A. Wallraff, A. Isacsson, and A. Bachtold, Energy-dependent path of dissipation in nanomechanical resonators, Nat. Nanotechnol. **12**, 631 (2017).

[12] M. Wang, D. J. Perez-Morelo, D. Lopez, and V. A. Aksyuk, Persistent nonlinear phase-locking and nonmonotonic energy dissipation in micromechanical resonators, Phys. Rev. X **12**, 041025 (2022).

[13] O. Shoshani, S. W. Shaw, and M. I. Dykman, Anomalous decay of nanomechanical modes going through nonlinear resonance, Sci. Rep. **7**, 18091 (2017).

[14] B. H. Schneider, V. Singh, W. J. Venstra, H. B. Meerwaldt, and G. A. Steele, Observation of decoherence in a carbon nanotube mechanical resonator, Nat. Commun. **5**, 5819 (2014).

[15] M. I. Dykman and M. A. Krivoglaz, Spectral distribution of nonlinear oscillators with nonlinear friction due to a medium, Phys. Stat. Sol. (b) **68**, 111 (1975).

[16] A. Eichler, J. Moser, J. Chaste, M. Zdrojek, I. Wilson-Rae, and A. Bachtold, Nonlinear damping in mechanical resonators made from carbon nanotubes and graphene, Nat. Nanotechnol. **6**, 339 (2011).

[17] P. M. Polunin, Y. Yang, M. I. Dykman, T. W. Kenny, and S. W. Shaw, Characterization of MEMS resonator nonlinearities using the ringdown response, J. Microelectromech. Syst. **25**, 297 (2016).

[18] L. Catalini, M. Rossi, E. C. Langman, and A. Schliesser, Modeling and observation of nonlinear damping in dissipation-diluted nanomechanical resonators, Phys. Rev. Lett. **126**, 174101 (2021).

[19] L. Sementilli, D. M. Lukin, H. Lee, J. Yang, E. Romero, J. Vučković, and W. P. Bowen, Low-dissipation nanomechanical devices from monocrystalline silicon carbide, Nano Lett. **25**, 6069 (2025).

[20] J. S. Huber, G. Rastelli, M. J. Seitner, J. Kölbl, W. Belzig, M. I. Dykman, and E. M. Weig, Spectral evidence of squeezing of a weakly damped driven nanomechanical mode, Phys. Rev. X **10**, 021066 (2020).

[21] J. S. Ochs, M. Seitner, M. I. Dykman, and E. M. Weig, Amplification and spectral evidence of squeezing in the response of a strongly driven nanoresonator to a probe field, Phys. Rev. A **103**, 013506 (2021).

[22] F. Yang, M. Fu, B. Bosnjak, R. H. Blick, Y. Jiang, and E. Scheer, Mechanically modulated sideband and squeezing effects of membrane resonators, Phys. Rev. Lett. **127**, 184301 (2021).

[23] B. Zhang, Y. Yan, X. Dong, M. I. Dykman, and H. Chan, Frequency stabilization of self-sustained oscillations in a sideband-driven electromechanical resonator, Phys. Rev. Appl. **22**, 034072 (2024).

[24] S. Houri, M. Asano, H. Okamoto, and H. Yamaguchi, Self-sustained libration regime in nonlinear microelectromechanical devices, Phys. Rev. Appl. **16**, 064015 (2021).

[25] D. A. Czaplewski, C. Chen, D. Lopez, O. Shoshani, A. M. Eriksson, S. Strachan, and S. W. Shaw, Bifurcation generated mechanical frequency comb, Phys. Rev. Lett. **121**, 244302 (2018).

[26] M. I. Dykman, G. Rastelli, M. L. Roukes, and E. M. Weig, Resonantly induced friction and frequency combs in driven nanomechanical systems, Phys. Rev. Lett. **122**, 254301 (2019).

[27] J. S. Ochs, D. K. J. Boneß, G. Rastelli, M. Seitner, W. Belzig, M. I. Dykman, and E. M. Weig, Frequency comb from a single driven nonlinear nanomechanical mode, Phys. Rev. X **12**, 041019 (2022).

[28] A. Keşkekler, H. Arjmandi-Tash, P. G. Steeneken, and F. Alijani, Symmetry-breaking-induced frequency combs in graphene resonators, Nano Lett. **22**, 6048 (2022).

[29] M. H. J. d. Jong, A. Ganesan, A. Cupertino, S. Gröblacher, and R. A. Norte, Mechanical overtone frequency combs, Nat. Commun. **14**, 1458 (2023).

[30] X. Wang, Q. Yang, R. Huan, Z. Shi, W. Zhu, Z. Jiang, Z. Deng, and X. Wei, Frequency comb in 1:3 internal resonance of coupled micromechanical resonators, Appl. Phys. Lett. **120**, 173506 (2022).

[31] R. Singh, A. Sarkar, C. Guria, R. J. Nicholl, S. Chakraborty, K. I. Bolotin, and S. Ghosh, Giant tunable mechanical nonlinearity in graphene–silicon nitride hybrid resonator, Nano Lett. **20**, 4659 (2020).

[32] H. Mouharrar, S. Rahmanian, R. Abdelrahman, Y. S. Shama, M. Akbari, M. Yavuz, and E. Abdel-Rahman, Generation of soliton frequency combs in NEMS, Nano Lett. **24** 10834 (2024).

[33] S. Houri, M. Asano, H. Yamaguchi, N. Yoshimura, Y. Koike, and L. Minati, Generic rotating-frame-based approach to chaos generation in nonlinear micro- and nanoelectromechanical system resonators, Phys. Rev. Lett. **125**, 174301 (2020).

[34] M. Defoort, L. Rufer, L. Fesquet, and S. Basrour, A dynamical approach to generate chaos in a micromechanical resonator, Microsyst. Nanoeng. **7**, 17 (2021).

[35] O. Shoshani and S. W. Shaw, Nonlinear interactions between vibration modes with vastly different eigenfrequencies, Commun. Phys. **6**, 213 (2023).

[36] A. M. Eriksson, O. Shoshani, D. López, S. W. Shaw, and D. A. Czaplewski, Controllable branching of robust response patterns in nonlinear mechanical resonators, Nat. Commun. **14**, 161 (2023).

[37] S. Houri, D. Hatanaka, M. Asano, R. Ohta, and H. Yamaguchi, Limit cycles and bifurcations in a nonlinear MEMS resonator with a 1:3 internal resonance, Appl. Phys. Lett. **114**, 103103 (2019).

[38] W. Luo, N. Gao, and D. Liu, Multimode nonlinear coupling induced by internal resonance in a microcantilever resonator, Nano Lett. **21**, 1062 (2021).

[39] D. A. Czaplewski, S. Strachan, O. Shoshani, S. W. Shaw, and D. López, Bifurcation diagram and dynamic response of a MEMS resonator with a 1:3 internal resonance, Appl. Phys. Lett. **114**, 254104 (2019).

[40] M. Bückle, Y. S. Klaß, F. B. Nägele, R. Braive, and E. M. Weig, Universal length dependence of tensile stress in nanomechanical string resonators, Phys. Rev. Appl. **15**, 034063 (2021).

[41] Y. S. Klaß, J. Doster, M. Bückle, R. Braive, and E. M. Weig, Determining Young's modulus via the eigenmode spectrum of a nanomechanical string resonator, Appl. Phys. Lett. **121**, 083501 (2022).

[42] J. S. Ochs, G. Rastelli, M. Seitner, M. I. Dykman, and E. M. Weig, Resonant nonlinear response of a nanomechanical system with broken symmetry, Phys. Rev. B **104**, 155434 (2021).

[43] L. D. Landau and E. M. Lifshitz, *Mechanics*, 2nd ed. (Pergamon Press, Oxford, 1976), Vol. 1.

[44] See Supplemental Material at http://link.aps.org/supplemental/10.1103/xhll-lhcj for the definition of the maximal deviation; how the phase-space trajectories decay in the rotating frame; description of the quasiconservative dynamics; the frequency-energy relation shown in Fig. 2; the experimental method of ringdown measurement; a qualitative understanding of strong nonlinearity via case comparisons; other weak nonlinear corrections; and a comparison of noise floor and relaxation, which includes Refs. [45–47].

[45] J. Guckenheimer and P. J. Holmes, *Nonlinear Oscillations, Dynamical Systems, and Bifurcations of Vector Fields* (Springer, New York, 2013).

[46] A. N. Cleland and M. L. Roukes, Fabrication of high frequency nanometer scale mechanical resonators from bulk Si crystals, Appl. Phys. Lett. **69**, 2653 (1996).

[47] Zurich Instruments, Principles of lock-in detection, Technical Report (Zurich instruments AG, Zurich, Switzerland, 2023).

[48] C. S. Barquist, W. G. Jiang, K. Gunther, N. Eng, Y. Lee, and H. B. Chan, Damping of a microelectromechanical oscillator in turbulent superfluid ^{4}He: A probe of quantized vorticity in the ultralow temperature regime, Phys. Rev. B **101**, 174513 (2020).

[49] A. Guthrie, S. Kafanov, M. T. Noble, Y. A. Pashkin, G. R. Pickett, V. Tsepelin, A. A. Dorofeev, V. A. Krupenin, and D. E. Presnov, Nanoscale real-time detection of quantum vortices at millikelvin temperatures, Nat. Commun. **12**, 2645 (2021).

[50] C. S. Barquist, W. G. Jiang, K. Gunther, Y. Lee, and H. B. Chan, Phase noise in a Duffing oscillator induced by quantum turbulence, Phys. Rev. B **106**, 094502 (2022).

Supplemental Material: Non-Exponential Relaxation in the Rotating Frame of a Driven Nanomechanical Mode

Hyunjin Choi, Oriel Shoshani, Ryundon Kim, Younghun Ryu, Jinhoon Jeong, Junho Suh, Steven W. Shaw, M. I. Dykman, and Hyoungsoon Choi

S.1. THEORY

The equations of motion in the rotating frame, $\dot{q} = \partial_p \mathcal{H} - \Gamma q$, $\dot{p} = -\partial_q \mathcal{H} - \Gamma p$ is obtained by adding linear damping to the Hamiltonian $\mathcal{H}_0$ and $\mathcal{H}_1$ given in the main text with

$$\mathcal{H}_0(q,p) = \frac{3\gamma}{32\omega_1}(q^2+p^2)^2 - \frac{1}{2}\delta\omega_1(q^2+p^2) - \frac{F_1 q}{2\omega_1},$$
$$\mathcal{H}_1(q,p,t) = -F_2[q\cos(\delta\omega_2 t) + p\sin(\delta\omega_2 t)]/2\omega_1.$$

The equations are then written explicitly as

$$\dot{q} = -\left(\delta\omega_1 - \frac{3\gamma}{8\omega_1}(q^2+p^2)\right)p - \frac{F_2}{2\omega_1}\sin(\delta\omega_2 t) - \Gamma q, \tag{S1}$$

$$\dot{p} = \left(\delta\omega_1 - \frac{3\gamma}{8\omega_1}(q^2+p^2)\right)q + \frac{F_1}{2\omega_1} + \frac{F_2}{2\omega_1}\cos(\delta\omega_2 t) - \Gamma p. \tag{S2}$$

The conservative dynamics ($\Gamma = 0$, $F_2 = 0$) can be viewed as the motion of a "particle" with position q, "momentum" p and Hamiltonian $\mathcal{H}_0$. Therefore, when $\gamma > 0$ and $\delta\omega_1 > 0$, the extrema of $\mathcal{H}_0$ correspond to the equilibrium points of the particle for which $p = 0$, and $q = q_{\rm eq}$. These equilibrium points are found by solving the algebraic equation

$$\frac{F_1}{2\omega_1} - \frac{3\gamma}{8\omega_1}q_{\rm eq}^3 + \delta\omega_1 q_{\rm eq} = 0. \tag{S3}$$

For $F_1 > F_{\rm cr_1}$, this equation has three real solutions. A straightforward linear stability analysis shows that the determinant of the corresponding Jacobian is given by $\Delta = \partial_q^2\mathcal{H}_0|_{(q_{\rm eq},0)}\partial_p^2\mathcal{H}_0|_{(q_{\rm eq},0)}$, which is positive for the intermediate and largest solutions of Eq. (S3), and negative for the smallest solution. Therefore, the intermediate and largest equilibrium points are centers, and the smallest equilibrium point is a saddle. We focus here on cases where the inclusion of $\mathcal{H}_1$ ($F_2 \neq 0$) and the light damping Γ lead to oscillations in the vicinity of the stable high-amplitude state $(a_{\rm hi}, 0)$ where $a_{\rm hi}$ can be approximated by

$$a_{\rm hi} \equiv q_{\rm eq} \approx \sqrt{\frac{8\omega_1\delta\omega_1}{3\gamma} + F_1\sqrt{\frac{2}{3\gamma\omega_1\delta\omega_1}}}. \tag{S4}$$

The amplitude approximation in Eq. (S4) is shown in Fig. 1(b) of the main text and agrees well with the experimental measurements.

To analyze the oscillations around $(q_{\rm eq}, 0)$, we introduce the local coordinate $u = q - q_{\rm eq}$, which yields the following dynamical system for the deviation away from the high-amplitude state

$$\dot{u} = \left(\frac{3\gamma q_{\rm eq}^2}{8\omega_1} - \delta\omega_1\right)p + \frac{3\gamma}{8\omega_1}\left[p^2 + u(u+2q_{\rm eq})\right]p - \frac{F_2}{2\omega_1}\sin(\delta\omega_2 t) - \Gamma u, \tag{S5}$$

$$\dot{p} = -\left(\frac{9\gamma q_{\rm eq}^2}{8\omega_1} - \delta\omega_1\right)u - \frac{3\gamma}{8\omega_1}\left[p^2(q_{\rm eq}+u) + u^2(u+3q_{\rm eq})\right] + \frac{F_2}{2\omega_1}\cos(\delta\omega_2 t) - \Gamma p. \tag{S6}$$

The eigenfrequency of small deviations ($|u|, |p| \ll q_{\rm eq}$) is given by

$$\Omega = \sqrt{\left(\frac{3\gamma q_{\rm eq}^2}{8\omega_1} - \delta\omega_1\right)\left(\frac{9\gamma q_{\rm eq}^2}{8\omega_1} - \delta\omega_1\right)} = \sqrt{\frac{F_1}{32\omega_1^2}\left(\frac{9\gamma F_1}{\omega_1\delta\omega_1} + 8\sqrt{6\gamma\omega_1\delta\omega_1}\right)}.$$

For a near-resonant secondary drive $|\delta\omega_2 - \Omega|/\Omega \ll 1$, u and p can oscillate non-linearly with large amplitude around $(q_{\rm eq}, 0)$. When the secondary drive is weak, $F_2 \ll F_1$, we can apply a standard perturbation analysis of weakly

nonlinear oscillators. To this end, we introduce a bookkeeping parameter ϵ to keep track of small quantities in Eqs. (S5)-(S6)

$$\dot{u} = \left(\frac{3\gamma q_{\rm eq}^2}{8\omega_1} - \delta\omega_1\right) p + \frac{3\gamma}{8\omega_1}\left[p^2 + u(u+2q_{\rm eq})\right] p - \frac{\epsilon^3 F_2}{2\omega_1}\sin(\delta\omega_2 t) - \epsilon^2\Gamma u, \tag{S7}$$

$$\dot{p} = -\left(\frac{9\gamma q_{\rm eq}^2}{8\omega_1} - \delta\omega_1\right) u - \frac{3\gamma}{8\omega_1}\left[p^2(q_{\rm eq}+u)+u^2(u+3q_{\rm eq})\right] + \frac{\epsilon^3 F_2}{2\omega_1}\cos(\delta\omega_2 t) - \epsilon^2\Gamma p, \tag{S8}$$

and use the asymptotic expansion

$$u(t) = \epsilon u^{(1)}(t,\epsilon^2 t) + \epsilon^2 u^{(2)}(t,\epsilon^2 t) + \epsilon^3 u^{(3)}(t,\epsilon^2 t) + \mathcal{O}(\epsilon^4),\ p(t) = \epsilon p^{(1)}(t,\epsilon^2 t) + \epsilon^2 p^{(2)}(t,\epsilon^2 t) + \epsilon^3 p^{(3)}(t,\epsilon^2 t) + \mathcal{O}(\epsilon^4),$$

where we explicitly denote the presence of a slow time-scale $\epsilon^2 t$ that is associated with the relaxation time of the system $1/(\epsilon^2\Gamma)$. By substituting the asymptotic expansion into Eqs. (S7)-(S8), rearranging them, and equating the same power of ϵ to zero, we obtain the following set of equations:

$$\mathcal{O}(\epsilon):\ \ddot{u}^{(1)} + \Omega^2 u^{(1)} = 0, \tag{S9}$$

$$\mathcal{O}(\epsilon^2):\ \ddot{u}^{(2)} + \Omega^2 u^{(2)} = \frac{3\gamma q_{\rm eq}}{64\omega_1^2}\left[(8\omega_1\delta\omega_1 - 3\gamma q_{\rm eq}^2)(3u^{(1)2} + p^{(1)2}) + 16\omega_1(u^{(1)}\dot{p}^{(1)} + \dot{u}^{(1)}p^{(1)})\right], \tag{S10}$$

$$\begin{aligned}\mathcal{O}(\epsilon^3):\ \ddot{u}^{(3)} + \Omega^2 u^{(3)} = {}& \frac{F_2[\omega_1(\delta\omega_2 - \delta\omega_1) + 3\gamma q_{\rm eq}^2]}{16\omega_1^2}\cos(\delta\omega_2 t) - 2\partial_{\epsilon^2 t}\dot{u}^{(1)} - \Gamma\left[\dot{u}^{(1)} + \left(\frac{3\gamma q_{\rm eq}^2}{8\omega_1} - \delta\omega_1\right)p^{(1)}\right] \\ & + \frac{3\gamma q_{\rm eq}}{4\omega_1}\left[u^{(2)}\dot{p}^{(1)} + \dot{u}^{(2)}p^{(1)} + u^{(1)}\dot{p}^{(2)} + \dot{u}^{(1)}p^{(2)} - \left(\frac{3\gamma q_{\rm eq}^2}{8\omega_1} - \delta\omega_1\right)(3u^{(1)}u^{(2)} + p^{(1)}p^{(2)})\right] \\ & + \frac{3\gamma}{8\omega_1}\left[\dot{p}^{(1)}(3p^{(1)2} + u^{(1)2}) + 2u^{(1)}p^{(1)}\dot{u}^{(1)} + \left(\frac{3\gamma q_{\rm eq}^2}{8\omega_1} - \delta\omega_1\right)u^{(1)}(p^{(1)2} - u^{(1)2})\right],\end{aligned} \tag{S11}$$

where $p^{(j)}$ can be computed from the following expressions

$$\left(\frac{3\gamma q_{\rm eq}^2}{8\omega_1} - \delta\omega_1\right)p^{(1)} = \dot{u}^{(1)}, \qquad \left(\frac{3\gamma q_{\rm eq}^2}{8\omega_1} - \delta\omega_1\right)p^{(2)} = \dot{u}^{(2)} - \frac{3\gamma q_{\rm eq}}{4\omega_1}p^{(1)}u^{(1)},$$

$$\left(\frac{3\gamma q_{\rm eq}^2}{8\omega_1} - \delta\omega_1\right)p^{(3)} = \dot{u}^{(3)} + \Gamma u^{(1)} - \frac{F_2}{2\omega_1}\sin(\delta\omega_2 t) + \frac{3\gamma}{8\omega_1}\left[2q_{\rm eq}(u^{(1)}p^{(2)} + u^{(2)}p^{(1)}) + p^{(1)}(p^{(1)2} + u^{(1)2})\right].$$

The solution of Eq. (S9) is given by $u^{(1)}(t,\epsilon^2 t) = a(\epsilon^2 t)\cos(\Omega t + \phi(\epsilon^2 t))$, which can be substituted into Eqs. (S10)-(S11) to determine $u^{(2)}$, $u^{(3)}$, and a pair of slow evolution equations for $a(\epsilon^2 t)$ and $\phi(\epsilon^2 t)$ [from the fundamental harmonic components in Eq. (S11)]. By defining a modified phase $\theta = -\phi + (\delta\omega_2 - \Omega)t$, which implies a resonant secondary drive $|\delta\omega_2 - \Omega| \sim \mathcal{O}(\epsilon^2)$, we arrive to the following slow evolution equations

$$\frac{da}{d(\epsilon^2 t)} = -\Gamma a - \frac{F_{2\rm eff}}{4\omega_1}\sin\theta, \tag{S12}$$

$$\frac{d\theta}{d(\epsilon^2 t)} = \Omega - \delta\omega_2 + \frac{3\gamma_{\rm eff}}{8\Omega}a^2 - \frac{F_{2\rm eff}}{4\omega_1 a}\cos\theta, \tag{S13}$$

where

$$\gamma_{\rm eff} = \frac{\gamma(-81\gamma^3 q_{\rm eq}^6 - 504\gamma^2 q_{\rm eq}^4\omega_1\delta\omega_1 + 576\gamma q_{\rm eq}^2\omega_1^2\delta\omega_1^2 + 512\omega_1^3\delta\omega_1^3)}{1024\omega_1^4\Omega^2} \text{ and } F_{2\rm eff} = F_2\left(1 + \sqrt{\frac{8\omega_1\delta\omega_1 - 3\gamma q_{\rm eq}^2}{8\omega_1\delta\omega_1 - 9\gamma q_{\rm eq}^2}}\right) \tag{S14}$$

represent the effective Duffing coefficient of the response and the effective drive amplitude of the in-phase component, respectively. We note that while Eqs. (S12)-(S13) represent oscillations in the rotating frame around $(q_{\rm eq}, 0)$, their structure is similar to the structure of the phase and amplitude equations of a standard Duffing oscillator. Therefore, the same techniques can be applied to analyze these equations and we find the threshold drive amplitude $F_{\rm cr_2}$ given by

$$F_{\rm cr_2} = \frac{32}{1 + \sqrt{(8\omega_1\delta\omega_1 - 3\gamma q_{\rm eq}^2)/(8\omega_1\delta\omega_1 - 9\gamma q_{\rm eq}^2)}}\sqrt{\Omega\omega_1^2\Gamma^3/(9\sqrt{3}|\gamma_{\rm eff}|)}$$

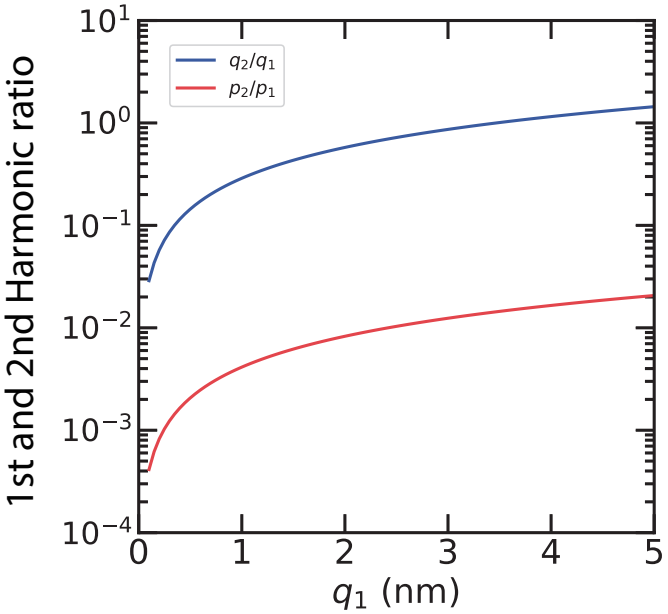

Fig. S1. Ratio of the second to first harmonic amplitudes as a function of q_1. The blue(q) and red(p) lines are calculated from Eq. (S15) and (S16), respectively.

such that bi-stable response exists for $F_2 > F_{\mathrm{cr}_2}$. With the inclusion of a DC offset and the secondary overtone, the expressions for u and p are given by

$$u = \frac{3\gamma q_{\mathrm{eq}} a^2 (16\omega_1\delta\omega_1 - 9\gamma q_{\mathrm{eq}}^2)}{(8\omega_1\delta\omega_1 - 9\gamma q_{\mathrm{eq}}^2)(8\omega_1\delta\omega_1 - 3\gamma q_{\mathrm{eq}}^2)} + a\cos(\delta\omega_2 t - \theta)$$
$$- \frac{6\gamma q_{\mathrm{eq}} a^2 (4\omega_1\delta\omega_1 - 3\gamma q_{\mathrm{eq}}^2)}{(8\omega_1\delta\omega_1 - 9\gamma q_{\mathrm{eq}}^2)(8\omega_1\delta\omega_1 - 3\gamma q_{\mathrm{eq}}^2)} \cos(2\delta\omega_2 t - 2\theta), \tag{S15}$$

$$p = \frac{8\omega_1 a}{8\omega_1\delta\omega_1 - 3\gamma q_{\mathrm{eq}}^2} [\delta\omega_2 \sin(\delta\omega_2 t - \theta) - \Gamma\cos(\delta\omega_2 t - \theta)] + \frac{4F_2}{8\omega_1\delta\omega_1 - 3\gamma q_{\mathrm{eq}}^2} \sin(\delta\omega_2 t)$$
$$+ \frac{24\gamma q_{\mathrm{eq}}\omega_1\delta\omega_2 a^2}{(8\omega_1\delta\omega_1 - 9\gamma q_{\mathrm{eq}})(8\omega_1\delta\omega_1 - 3\gamma q_{\mathrm{eq}})} \sin(2\delta\omega_2 t - 2\theta). \tag{S16}$$

Note that Eqs. (S15)-(S16) can also describe the ring-down response with F_2 set to zero, and the frequency and amplitude replaced by $\delta\omega_2 \to \Omega$ and $a \to a(0)\mathrm{e}^{-\Gamma t}$. Therefore, we see that while the fundamental harmonic decays with $\mathrm{e}^{-\Gamma t}$, the second harmonic and the DC offset decay with $\mathrm{e}^{-2\Gamma t}$.

The threshold maximal deviation δq at which the 2Γ decay contribution becomes negligible can be estimated from Eq. S15 and Eq. S16. The ratios of the second to first harmonic amplitudes, q_2/q_1 and p_2/p_1, calculated from these equations are plotted as a function of q_1. Using a practical criterion $q_2/q_1 < 0.1$ for the disappearance of the 2Γ component, we find that this occurs at maximal deviations δq of a few hundred picometers. Meanwhile, p_2/p_1 remains sufficiently small, indicating that the 2Γ decay is already negligible in the p. This behavior is consistent with Fig. 3(b), where the decay transitions to the Γ regime as δq approaches the hundred-picometer scale.

An alternative and more global way to describe the dynamics is by using an action-angle representation of the oscillations in the rotating frame, where $I_{\mathrm{ho}} = (q^2 + p^2)/2$ is the action, and $\tan^{-1}(p/q) = \phi_{\mathrm{ho}}$ is the angle. The

Hamiltonian $\mathcal{H}_0$ and the evolution equations of the action and angle are given by

$$\mathcal{H}_0 = -\Delta\omega_1 I_{\rm ho} + \frac{3\gamma}{8\omega_1} I_{\rm ho}^2 - \frac{F_1}{\omega_1}\sqrt{\frac{I_{\rm ho}}{2}}\cos\phi_{\rm ho} \tag{S17}$$

$$\begin{aligned}\dot{\phi}_{\rm ho} &= \frac{\partial \mathcal{H}_0}{\partial I_{\rm ho}} - \mathcal{F}_{\phi_{\rm ho}} \\ &= -\Delta\omega_1 + \frac{3\gamma}{4\omega_1} I_{\rm ho} - \frac{1}{2\omega_1\sqrt{2I_{\rm ho}}}[F_1\cos\phi_{\rm ho} + F_2\cos(\Delta\omega_2 t - \phi_{\rm ho})],\end{aligned} \tag{S18}$$

$$\begin{aligned}\dot{I}_{\rm ho} &= -\frac{\partial \mathcal{H}_0}{\partial \phi_{\rm ho}} - \mathcal{F}_{I_{\rm ho}} \\ &= -\frac{\sqrt{2I_{\rm ho}}}{2\omega_1}[F_1\sin\phi_{\rm ho} - F_2\sin(\Delta\omega_2 t - \phi_{\rm ho})] - 2\Gamma I_{\rm ho}.\end{aligned} \tag{S19}$$

For $\Gamma = 0, F_2 = 0$, Eqs. (S17)-(S19) can be readily integrated, and the action dynamics can be simply visualized as the motion of a "particle" trapped in a potential well of a particular shape. To see this, we simply square and add Eq. (S17) and Eq. (S19) to get

$$\frac{\dot{I}_{\rm ho}^2}{2} + U_{\rm eff}(I_{\rm ho}) = 0, \tag{S20}$$

where

$$U_{\rm eff}(I_{\rm ho}) = \frac{1}{2}\left(\mathcal{H}_0 + \Delta\omega_1 I_{\rm ho} - \frac{3\gamma I_{\rm ho}^2}{8\omega_1}\right)^2 - \left(\frac{F_1}{2\omega_1}\right)^2 I_{\rm ho}. \tag{S21}$$

Thus, the particle with action $I_{\rm ho}$ oscillates in the effective potential $U_{\rm eff}$ with zero effective total energy. The time dependence of $I_{\rm ho}$ can be written explicitly in terms of the Jacobi elliptic fucntions as

$$I_{\rm ho} = \frac{z_2 I_1 + z_1 I_2 - (z_2 I_1 - z_1 I_2)\mathrm{cn}(\tau - \tau_0)}{z_1 + z_2 - (z_1 - z_2)\mathrm{cn}(\tau - \tau_0)}, \tag{S22}$$

where $\tau = 3\pi\gamma\sqrt{z_1 z_2}t/[16\omega_1 K(m_{\mathcal{H}_0})]$, I_j's with $(j = 1, 2, 3, 4)$ are the roots of the equation $U_{\rm eff}(I_{\rm ho}) = 0$, $I_1 > I_2$ are real, $I_4 = I_3^*$ are complex conjugates, $z_j = \sqrt{(I_j - I_3)/(I_j - I_4)}$ with $(j = 1, 2)$, $K(m_{\mathcal{H}_0})$ is the complete elliptic integral of the first kind with the parameter $m_{\mathcal{H}_0} = [(I_1 - I_2)^2 - (z_1 - z_2)^2]/(4z_1 z_2)$, and τ_0 is set by the initial condition.

For small non-zero $\Gamma \ll \Omega$ and $F_2 \ll F_1$, the Hamiltonian $\mathcal{H}_0(I_{\rm ho}, \phi_{\rm ho})$ is no longer a constant of motion. However, the evolution of $\mathcal{H}_0$ can be found from

$$\dot{\mathcal{H}}_0 = -\left(\frac{\partial \mathcal{H}_0}{\partial \phi_{\rm ho}}\mathcal{F}_{\phi_{\rm ho}} + \frac{\partial \mathcal{H}_0}{\partial I_{\rm ho}}\mathcal{F}_{I_{\rm ho}}\right). \tag{S23}$$

As the right-hand side (RHS) of Eq. (S23) is small (of order Γ and F_2 in magnitude), its influence on $\mathcal{H}_0$ can be separated into two effects. The rapidly oscillating components cause only small-amplitude, high-frequency fluctuations(e.g., oscillate with the frequency Ω). In contrast, the slowly varying components drive a persistent drift that accumulates into a large, long-term change. Therefore, to isolate the dominant long-term dynamics, we neglect these fast-oscillating terms on the RHS of Eq. (S23). Neglecting the terms containing the fast oscillations ($\mathrm{e}^{in\Omega t}$, where $n = \pm 1, \pm 2, ...$) is equivalent to averaging over the period of the oscillations $T = 2\pi/\Omega$[1]; thus this method is often called the method of averaging. Hence, the averaged equation of $\mathcal{H}_0$ is given by

$$\langle\dot{\mathcal{H}}_0\rangle = -\left\langle\frac{\partial \mathcal{H}_0}{\partial \phi_{\rm ho}}\mathcal{F}_{\phi_{\rm ho}} + \frac{\partial \mathcal{H}_0}{\partial I_{\rm ho}}\mathcal{F}_{I_{\rm ho}}\right\rangle, \tag{S24}$$

where $\langle f\rangle = T^{-1}\int_0^T f dt$.

As explained in the main text and can be seen from Fig. S3(c), when both Γ and F_2 are non-zero, in steady-state they balance each other to produce a nearly constant $\langle\mathcal{H}_0\rangle$ for which $I_{\rm ho}$ oscillates periodically. As F_2 is increased, the value of $|\langle\mathcal{H}_0\rangle - \mathcal{H}_0(q_{\rm eq})|$ becomes larger and the amplitude of the attendant oscillations increases.

When $|[\mathcal{H}_0 - \mathcal{H}_0(q_{\rm eq})]/\mathcal{H}_0(q_{\rm eq})| \ll 1$, we find that $z_1 \approx z_2$; thus, Eq. (S22) can be approximated by $I_{\rm ho} \approx [I_1 + I_2 - (I_1 - I_2)\cos(\Omega t + \psi)]/2$, and Eq. (2) of the main text by $q - q_{\rm eq} \approx q_1\cos(\Omega t + \psi) + q_2\cos(2\Omega t + 2\psi)$, $p \approx p_1\sin(\Omega t + \psi)$.

A straightforward perturbation analysis reveals that in the presence of small damping ($\Gamma \ll \Omega$), q_1 and p_1 decay exponentially at the srate, *i.e.*, $q_1, p_1 \propto \mathrm{e}^{-\Gamma t}$, while q_2 decays exponentially at twice the rate, *i.e.*, $q_2 \propto \mathrm{e}^{-2\Gamma t}$. Consequently, when the lightly damped system is prepared with a fixed value of $\mathcal{H}_0$ that corresponds to fixed I_1 and I_2 such that $|[\mathcal{H}_0 - \mathcal{H}_0(q_{\mathrm{eq}})]/\mathcal{H}_0(q_{\mathrm{eq}})| \ll 1$, we calculate the ratio $q_2(0)/q_1(0) = [3\gamma(I_1 - I_2)/(32\omega_1)][\delta\omega_1 - 3\gamma(I_1 + I_2)/(8\omega_1)]^{-1}$. Thus, the decay of $q(t)$ towards q_{eq} is overall non-exponential and is dominated by a decay rate of 2Γ ($|q| \propto \mathrm{e}^{-2\Gamma t}$) when $[3\gamma(I_1 - I_2)/(32\omega_1)][\delta\omega_1 - 3\gamma(I_1 + I_2)/(8\omega_1)]^{-1} \gg 1$ and by a decay rate of Γ ($|q| \propto \mathrm{e}^{-\Gamma t}$) when $[3\gamma(I_1 - I_2)/(32\omega_1)][\delta\omega_1 - 3\gamma(I_1 + I_2)/(8\omega_1)]^{-1} \ll 1$.

S.2. PHASE-SPACE TRAJECTORIES IN THE ROTATING FRAME

The points of maximal deviation from equilibrium in the rotating frame phase space correspond to the lower and upper envelopes of the quadratures q and p, as illustrated in Fig. 3(a) of the main text and Fig. S2. The term "maximum" refers to a point where the first derivative of $|\delta q|$ is zero, the second derivative is negative, and, among the two such extrema in the upper panel of Fig. S2(a), the larger one is chosen. The attendant value of p is shown in the lower panel of Fig. S2(a). These maximal deviation points serve as reference markers for analyzing the decay behaviors of q and p during the ring-down process.

Another straightforward approach to analyzing the ring-down signal is to compare the experimental phase-space trajectories of (q, p) in the rotating frame with their theoretical counterparts and observe how these trajectories decay over time. The time evolution of the area $\mathcal{S}$, which is enclosed by the nearly-closed trajectories and is proportional to the action, can be obtained by using the divergence theorem to show that

$$\dot{I} \propto \dot{\mathcal{S}} = \oint_{\ell} \boldsymbol{f} \cdot \boldsymbol{n}\, d\ell = \int_{\mathcal{S}} \nabla \cdot \boldsymbol{f}\, d\mathcal{S} = -2\Gamma\mathcal{S}. \tag{S25}$$

In this expression, $I = (2\pi)^{-1} \oint p dq$ is the action associated with $\mathcal{H}_0$, $\boldsymbol{f} = (\dot{q}, \dot{p})^T$ represents the velocity vector in the phase portrait, $\boldsymbol{n}$ is the normal vector to the trajectory, and $d\ell$ is an infinitesimal segment of the closed trajectory. From Eq. S25 we find that $\mathcal{S}(t) = \mathcal{S}(0)e^{-2\Gamma t}$.

After switching off F_2, the area $\mathcal{S}$ decays as the system's trajectories contract within the rotating frame as shown in Fig. S2(c), (d). The logarithmic plot of $\mathcal{S}$ over time in Fig. 3(c) of the main text shows good agreement with the theoretical prediction, exhibiting a slope of $2\Gamma \approx 2.7\,\mathrm{Hz}$.

S.3. EXPERIMENTAL METHOD AND QUASI-CONSERVATIVE DYNAMICS

By applying an AC current in the presence of a perpendicular magnetic field, as depicted in Fig. 1(a) of the main text, the device is harmonically driven primarily via the Lorentz force and generates the electromotive force [2]. This signal is fed into a Zurich Instruments HF2LI lock-in amplifier, which demodulates the in-phase and quadrature components. A secondary drive is introduced to excite the sidebands by adding it to the output source of the lock-in amplifier. The sideband signal in the linear regime is measured using a second demodulator. In the nonlinear regime, a homodyne measurement was carried out to encapsulate the more complicated full dynamics of the system.

Strong nonlinearity has far-reaching consequences on the relaxation of the quadratures, which can be detected via homodyne measurement of $q(t)$ and $p(t)$ as shown in Fig. S3(a). In particular, the dynamics of $p(t)$ is dominated by its fundamental harmonic $p \propto \exp(\pm i\delta\omega_2 t)$ as shown in Fig. 4(d) of the main text. As a result, the overall spectrum of $x(t)$ in Fig. S3(b) are masked by considering only p.

An increase in the peak amplitude at ω_2 with increasing F_2 corresponds to higher-energy states in the rotating frame as captured by the system's low-pass filtered Hamiltonian level as shown in Fig. S3(c). The time-averaged Hamiltonian defined as $\langle\mathcal{H}_0\rangle = T_2^{-1}\int_0^{T_2}\mathcal{H}_0 dt$, serves as the horizontal axis variable for Fig. 4(c), (d) in the main text. The low-pass filtered Hamiltonian remains approximately constant at each drive level, shown in Fig. S3(c), indicating a quasi-conservative system due to the sideband damping being compensated by the secondary drive F_2.

S.4. FREQUENCY-ENERGY RELATION

Fig. 2(a) of the main text shows the results of a frequency sweep of the upper sideband in which ω_2 is varied, resulting in different energy states in the rotating frame. The figure shows only the amplitude of the first harmonic. However, because the system is strongly nonlinear, multiple harmonics must be considered to accurately capture the nonlinear response. To show this, we introduce the frequency-energy relation based on the conservative Hamiltonian

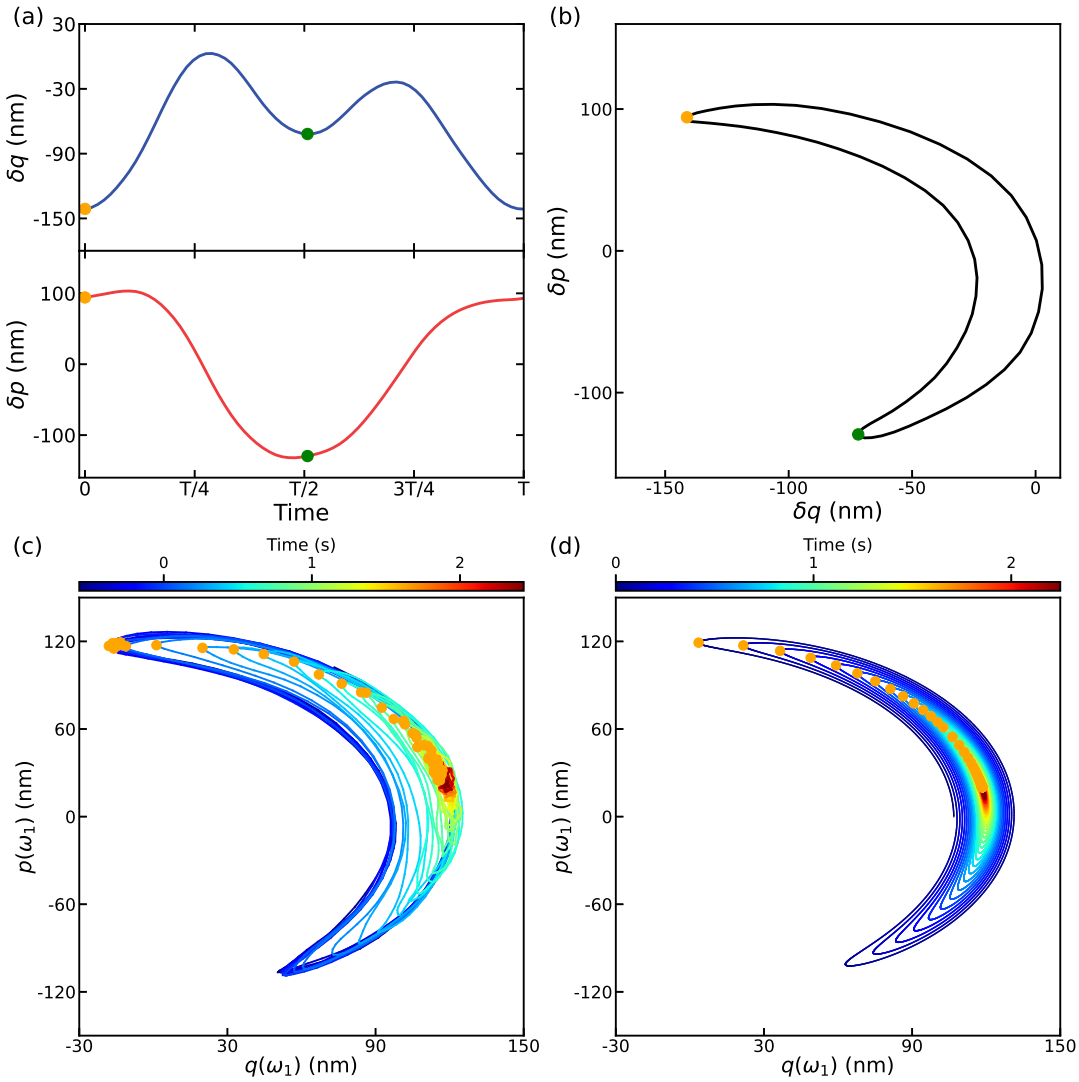

Fig. S2. (a) The oscillation of δq and δp within one cycle of the first harmonic frequency $T_2 = 2\pi/\delta\omega_2$, $\delta\omega_2/2\pi = 13$ Hz and $F_2 = 150\,\mathrm{mm/s^2}$, with the same values of $(F_1,\ \delta\omega_1)$ used for Fig. 3 of the main text. Orange and green circles indicate the extremal points. (b) Phase space trajectories in the rotating frame for the same cycle of (a) with the same extremal points indicated. Note that the orange circle represents the maximal deviation from equilibrium. (c),(d) Phase space trajectories in the rotating frame over time during the ring-down process, reconstructed from Fig. 3(a) of the main text, with the colormap representing the progression of time. Panels (c) and (d) show experimental and theoretical trajectories, respectively. The orange circles denote the points of maximal deviation from equilibrium in each cycle of the trajectory.

dynamics, neglecting damping so that the trajectories remain centered at $(q_{\mathrm{eq}}, 0)$. We observe that the effective resonance frequency in the rotating frame monotonically decreases as $\mathcal{H}_0$ increases, as depicted in Fig. S4(a). In the rotating frame phase space, the trajectories correspond to increasingly large, banana-shaped loops (Fig. S4(b)). Furthermore, higher-order harmonics of q become significant as $\mathcal{H}_0$ increases. Over the $\mathcal{H}_0$ values of interest the first and second harmonics dominate the response. Since these components have slower decay rates than the higher harmonics, they are essential for analyzing the ring-down behavior shown in Fig. 3 of the main text.

S.5. RING-DOWN MEASUREMENT

In the ring-down measurement presented in Fig. 1(c) of the main text, the system was initially driven in the Duffing nonlinear regime. After switching off the drive F_1, the demodulated signal at ω_0 was monitored using a sufficiently large bandwidth ($> \delta\omega_1$) to capture the full ring-down dynamics originating from the nonlinear state.

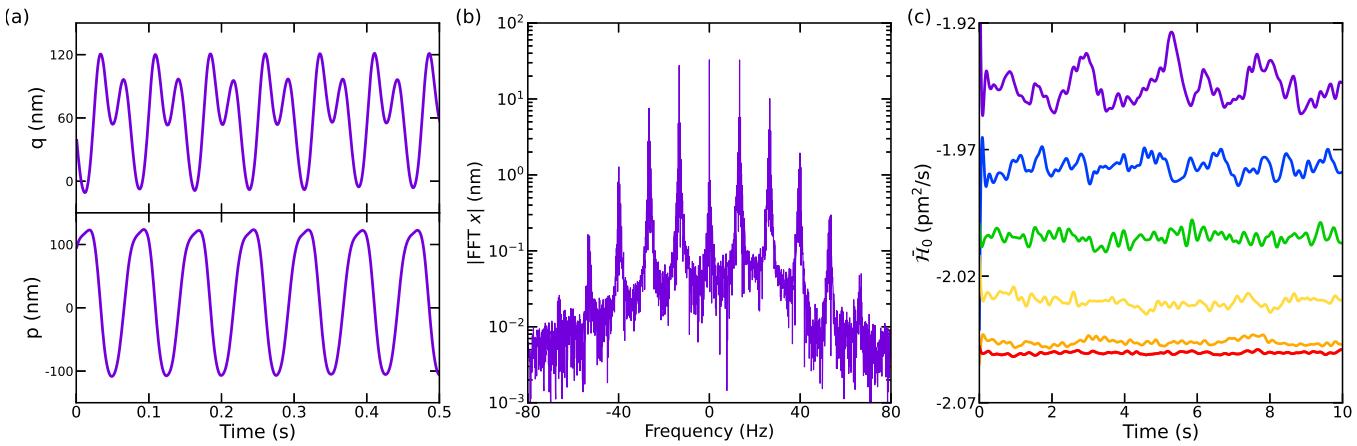

Fig. S3. (a) The top and bottom panels show the in-phase and quadrature components over time at the peak condition with $\delta\omega_2 = 13.3$ Hz and $F_2 = 150\,\mathrm{mm/s^2}$, corresponding to the purple-colored case in Fig.2 and Fig.4. of the main text. (b) The measured spectrum of $x(t) = q(t)\cos(\omega_1 t) + p(t)\sin(\omega_1 t)$ in the laboratory frame, using the $q(t)$ and $p(t)$ components shown in the top and bottom panels in (a). (c) The filtered Hamiltonian $\bar{\mathcal{H}}_0$ for each drive level of F_2, represented using the same rainbow colors in the main text, low-pass filtered with a cutoff frequency of 5 Hz. Drive levels are $F_2 = 15,\ 30,\ 60,\ 90,\ 120,$ and 150 mm/s^2.

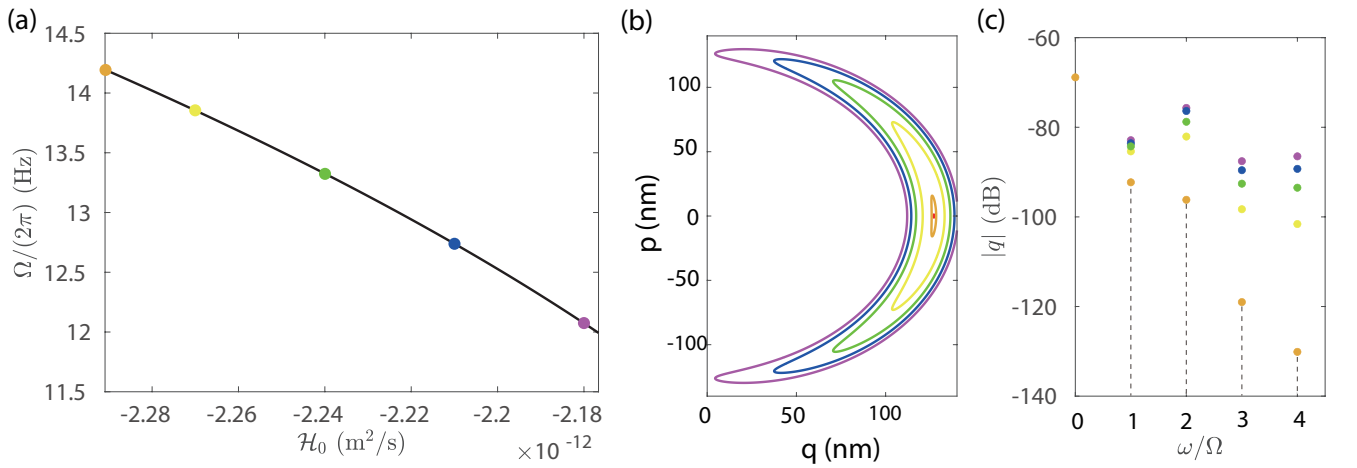

Fig. S4. (a) Effective resonance frequency in the rotating frame as a function of the conservative Hamiltonian $\mathcal{H}_0$. The Black line indicates the theoretical prediction, and the rainbow-colored circles denote representative points along the curve. (b) Theoretical phase-space trajectories in the rotating frame corresponding to the representative points in (a). (c) Theoretical harmonic components of q, plotted using the same color scheme as in (a)

In the ring-down measurement of the rotating frame, there exist two distinct time scales: the fast dynamics of the main tone at $\sim \omega_1^{-1}$ and the slower oscillatory motion at $\sim \delta\omega_2^{-1}$ and decay at $\sim \Gamma^{-1}$. Our real-time measurement technique is designed to track the slow dynamics of the motion, which oscillates at a frequency of $\delta\omega_2$.

To achieve this, we measure the real-time quadrature components $q(t)$ and $p(t)$, which are demodulated using reference signals $\cos(\omega_1 t)$ and $\sin(\omega_1 t)$. The key requirement is that the demodulator's bandwidth at ω_1 must be sufficiently broad to capture the full harmonic content of the slow dynamics, preventing any unintentional filtering of relevant signals[3]. In terms of time constant, which is inversely related to its bandwidth, the demodulator's time constant must be small enough to resolve the slow oscillations, *i.e.*, smaller than $\delta\omega_2^{-1}$.

For ring-down measurements, an additional constraint arises from the dissipation rate Γ. The demodulator's time constant must be shorter than the characteristic dissipation time $(2\Gamma)^{-1}$ of the oscillation. If the time constant is too large ($> (2\Gamma)^{-1}$), the demodulated signal becomes excessively smoothed, preventing accurate observation of the ringdown behavior.

As a concrete example in our system, for $\delta\omega_2/2\pi \sim 10$ Hz, we set the demodulator's time constant to 2 ms. This value is sufficiently small compared to both $(2\Gamma)^{-1} \sim 370$ ms and $\delta\omega_2^{-1} \sim 10$ ms, ensuring that our real-time

measurement method accurately captures the oscillatory motion and its decay dynamics.

S.6. QUALITATIVE UNDERSTANDING OF STRONG NONLINEARITY

To qualitatively understand the strong second harmonic of q, we decompose the effective Hamiltonian $\mathcal{H}_0$ into three parts: harmonic component $\mathcal{H}_L = \delta\omega_1(q^2+p^2)/2$, symmetric nonlinear component $\mathcal{H}_{NL} = 3\gamma(q^2+p^2)^2/32\omega_1$, and asymmetric component $\mathcal{H}_A = -F_1 q/2\omega_1$. The coefficients $\delta\omega_1$ and F_1 are key tunable parameters of the system's nonlinearity in the rotating frame, revealing a competing relationship between harmonicity (symmetry) and anharmonicity (asymmetry).

In Fig. 2(b) of the main text and Fig. S5(a), the estimated values at equilibrium ($q_{\rm eq}$, $p_{\rm eq}$) are $\mathcal{H}_L \sim -10^{-12}\,\mathrm{m^2Hz}$ and $\mathcal{H}_A \sim -10^{-13}\,\mathrm{m^2Hz}$, which are relatively comparable. As a result, when the system is driven sufficiently hard by F_2, the dynamics enter a nonlinear regime where $\mathcal{H}_A$, which depends solely on q, plays a key role in the emergence of the strong second harmonic of q. In contrast, for Fig. S5(b) where $\delta\omega_1/F_1$ is relatively large, these values shift to $\mathcal{H}_L \sim -10^{-7}\ \mathrm{m^2/s}$ and $\mathcal{H}_A \sim -10^{-12}\ \mathrm{m^2/s}$, making the anharmonic effects much weaker.

The secondary drive F_2 ranges from $15\,\mathrm{mm/s^2}$ to $150\,\mathrm{mm/s^2}$ for $\delta\omega_1 = 86.9\,\mathrm{Hz}$, $F_1 = 3.0\,\mathrm{m/s^2}$ in Fig. S5(a), and from $30\,\mathrm{mm/s^2}$ to $240\,\mathrm{mm/s^2}$ for $\delta\omega_1 = 18.4\,\mathrm{kHz}$, $F_1 = 60\,\mathrm{m/s^2}$ in Fig. S5 (b). For each F_2, the detuning of the secondary drive, $\delta\omega_2$, is chosen to correspond to the peak values (Fig. 2(a) in the main text). For small ratio $\delta\omega_1/F_1$ at equilibrium, the asymmetric term becomes comparable to the linear, leading to asymmetric trajectories in the phase space of the rotating frame. This results in a noticeable comparable contribution from the first and second harmonics, with the second harmonic of q becoming increasingly prominent (the upper panel of Fig. S5 (c)). For large detuning, the anharmonic term is relatively small, resulting in a more symmetric shape (Fig. S5(b)) and a weaker second-harmonic component of q (the upper panel of Fig. S5 (d)). This comparison explains why, in the case of Fig. S5(a), strong nonlinear behavior can be achieved with a relatively small secondary drive F_2, as the harmonic and asymmetric contributions remain comparable.

S.7. WEAK NONLINEAR CORRECTIONS: ASYMMETRIC POTENTIAL AND NONLINEAR DAMPING

In the analysis of the response to a resonant drive, the asymmetry in the heterostructure potential, which leads to odd terms such as $V(x) = \beta x^3 + \ldots$ in the nonlinear potential, can be accounted for by renormalizing the "bare" parameter of the quartic nonlinearity, unless the drive is so strong that the system approaches dynamical chaos in the laboratory frame [4].

We significantly expanded the range of the driving field amplitudes F_1, and thus of the amplitudes of forced vibrations, to investigate the influence of nonlinear damping. Such damping is usually modeled by the term $\Gamma_2 x^2\dot{x}$ in the laboratory frame. From the fitting shown in Fig. S6(a), the estimated nonlinear damping coefficient is $\Gamma_2 \simeq 6.34\times10^{12}\,\mathrm{m^{-2}s^{-1}}$. Following the same procedure described in the main text, we then apply a probe drive F_2 ($F_2/F_1 \sim 0.01$), and bring the system to the peak amplitude of the F_2-induced nonlinear vibrations in the rotating frame. We then examine how the quadratures q and p decay in the absence of F_2 as functions of the equilibrium amplitude of forced vibrations q_{eq}. The value of q_{eq} is changed by varying F_1 and $\delta\omega_1$.

Fig. S6(b) shows the initial (right after F_2 is switched off) decay rates of q (blue) and p (red) in the rotating frame, together with the decay rates $\Gamma + \Gamma_2 q_{eq}^2/4$ for p, and $2(\Gamma + \Gamma_2 q_{eq}^2/4)$ for q; the value $\Gamma + \Gamma_2 q_{eq}^2/4$ is the instantaneous decay rate of vibrations with amplitude q_{eq} in the laboratory frame in the presence of nonlinear friction. The results indicate that nonlinear damping can modify the decay rates in the rotating frame as q_{eq} increases to the values significantly higher than those studied in the main text, while still maintaining the approximately twofold faster decay of q compared to p.

In our main-text measurements, performed at $q_{eq} \simeq 0.127\,\mu\mathrm{m}$, the system operates in the small nonlinear-damping regime, as suggested by the trend in S6(b), where the effect of nonlinear damping is negligible and does not influence the main conclusions.

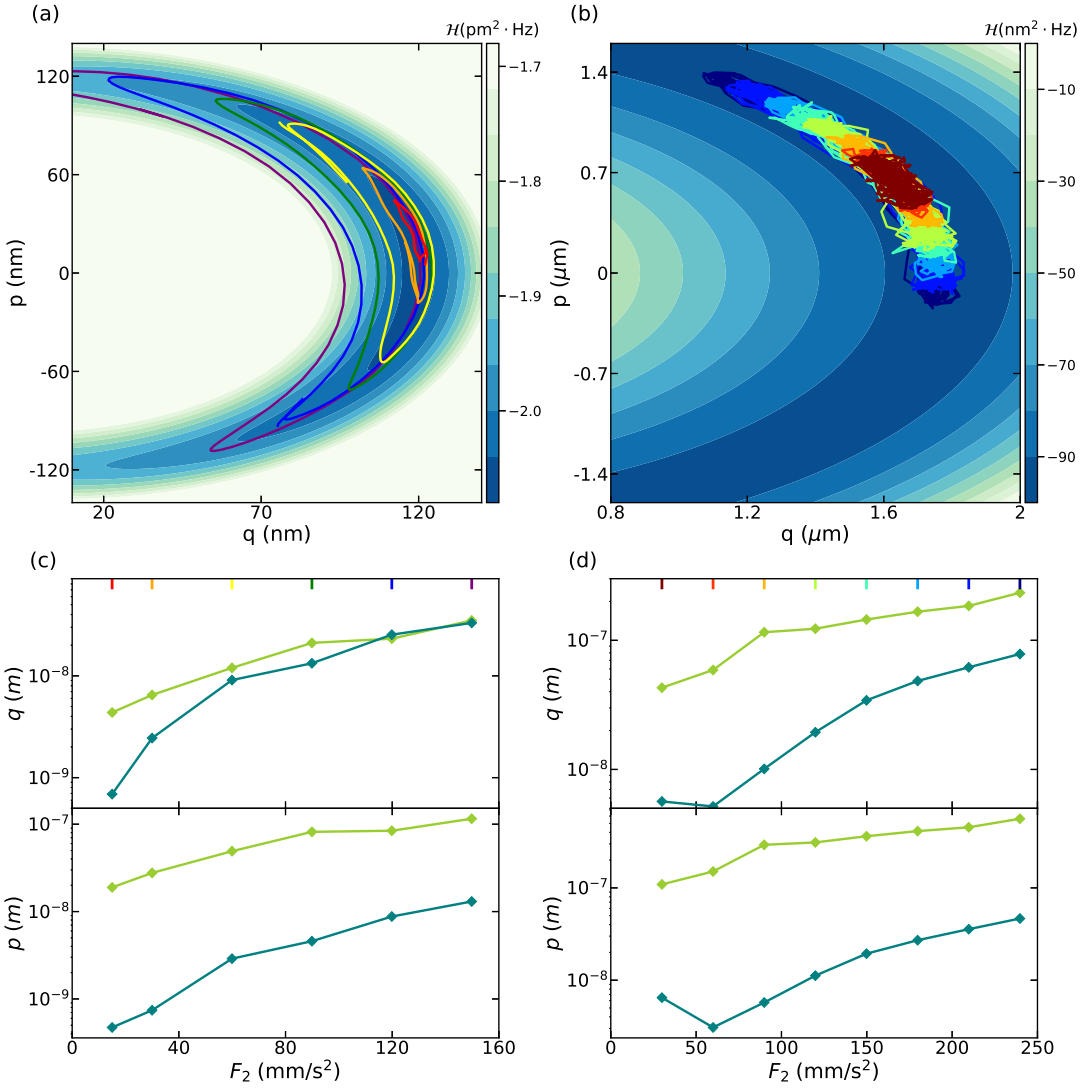

Fig. S5. Comparison of nonlinearities for small and large values of $\delta\omega_1/F_1$. (a), (c) correspond to the small case ($\delta\omega_1 = 86.9$ Hz, $F_1 = 3.0\,\mathrm{m/s^2}$), while (b), (d) correspond to the large case ($\delta\omega_1 = 18.4$ kHz, $F_1 = 60\,\mathrm{m/s^2}$). (a),(b) The phase space representation of the Hamiltonian $\mathcal{H}_0$ in the rotating frame near the equilibrium. Its contours represent constant Hamiltonian levels from the model, color-mapped accordingly. The maximum Hamiltonian levels of (a),(b) are capped differently for clear visualization of the region of interest. Rainbow-colored lines denote experimentally obtained trajectories at the peak condition by varying F_2 and $\delta\omega_2$. F_2 values are indicated on the x-axes of (c),(d), with the corresponding values marked on the upper x-axis of the top panels. (c),(d) First and second harmonic components of q and p as a function of F_2.

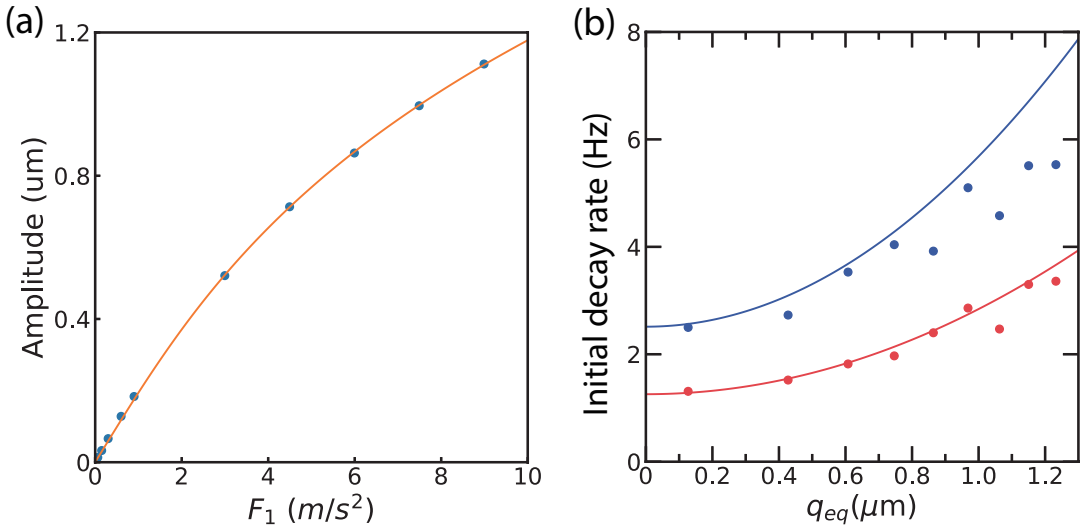

Fig. S6. (a) Peak amplitude as a function of F_1. The solid line shows the fitting curve. (b) Initial decay rates of q (blue) and p (red) as functions of q_{eq}, obtained from the ring-down measurements in the rotating frame. The solid lines represent the expected trends: $2(\Gamma + \Gamma_2 q_{eq}^2/4)$ (blue) for q and $\Gamma + \Gamma_2 q_{eq}^2/4$ (red) for p, derived from the effective decay rate $\Gamma + \Gamma_2 q_{eq}^2/4$ in the laboratory frame.

S.8. COMPARISON OF NOISE FLOOR AND RELAXATION

To assess the non-exponential relaxation relative to the noise floor and to clarify the range over which the experimental observations remain valid, we analyzed the tail of the ring-down signal for $t \geq 3\,\mathrm{s}$, which was not presented in the main text. Averaging this data with a $\pm 2\sigma$ interval defines the noise floor that contains 95% of the fluctuations, as shown in Fig. S7(a) and (b). The difference between the two noise levels arises from fluctuation-induced squeezing [5]. r As shown in Fig. S7(a), the experimental data enters the noise floor around $t \approx 2\,\mathrm{s}$. A clear deviation from both the 2Γ and Γ decay trends is observed in the range $0.5\,\mathrm{s} \leq t \leq 1.5\,\mathrm{s}$. For $t \geq 2.5\,\mathrm{s}$, the decay follows the Γ trend, although it becomes obscured by the noise floor.

[1] J. Guckenheimer and P. J. Holmes, *Nonlinear Oscillations, Dynamical Systems, and Bifurcations of Vector Fields* (Springer, New York, 2013).

[2] A. N. Cleland and M. L. Roukes, Fabrication of high frequency nanometer scale mechanical resonators from bulk si crystals, Applied Physics Letters **69**, 2653 (1996).

[3] Zurich Instruments, *Principles of Lock-in Detection*, Tech. Rep. (Zurich Instruments AG, Zurich, Switzerland, 2023).

[4] L. D. Landau and E. M. Lifshitz, *Mechanics*, 2nd ed., Vol. 1 (Pergamon Press, Oxford, 1976).

[5] J. S. Huber, G. Rastelli, M. J. Seitner, J. Kölbl, W. Belzig, M. I. Dykman, and E. M. Weig, Spectral Evidence of Squeezing of a Weakly Damped Driven Nanomechanical Mode, Physical Review X **10**, 021066 (2020), 1903.07601.

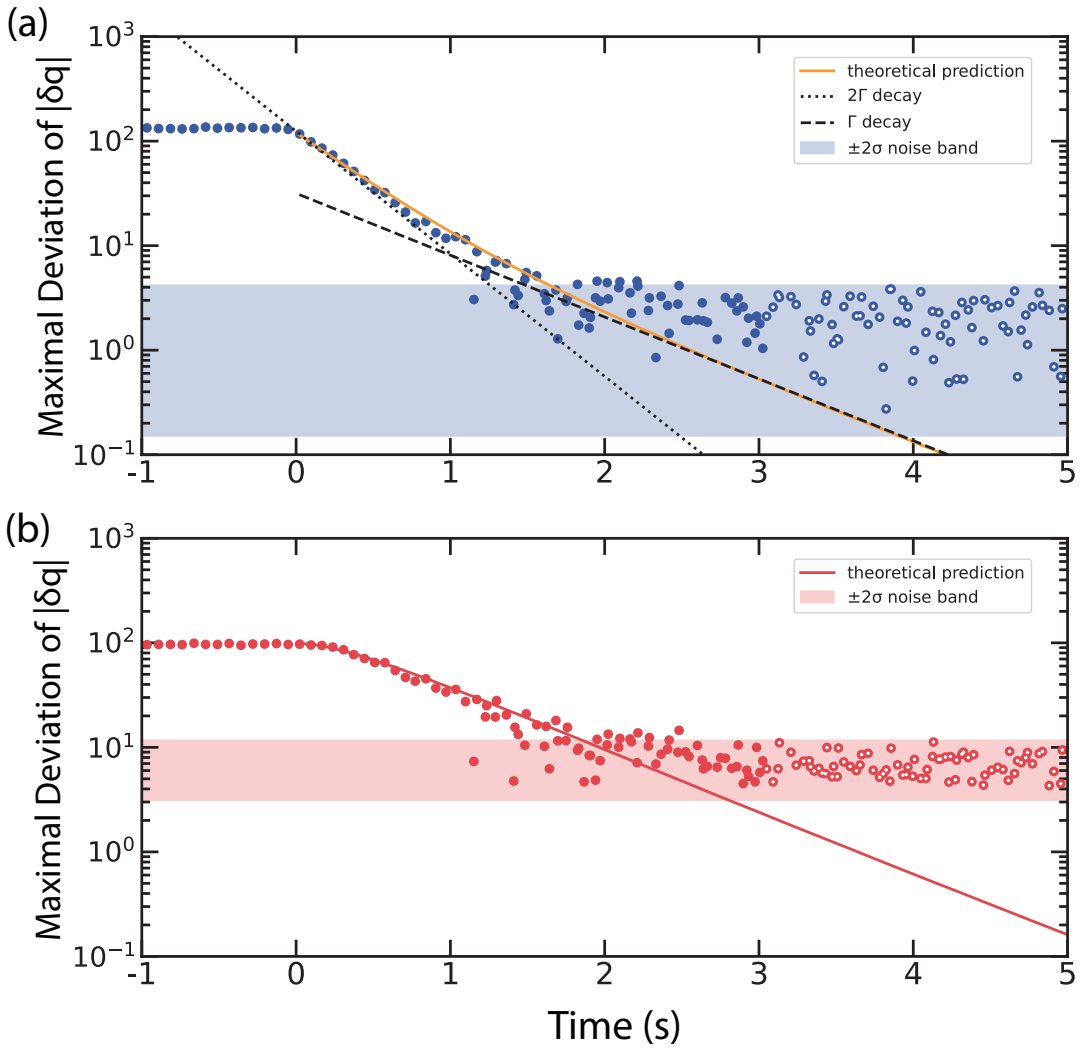

Fig. S7. Log–linear plot of the maximal deviations of δq (a) and δp (b) obtained from the ringdown measurements in the rotating frame, together with the noise floor. The shaded regions indicate the $\pm 2\sigma$ noise levels estimated from the tail data of the ringdown (open circles).